International Journal of Mechanical Sciences 151 (2019) 639–649

Contents lists available at ScienceDirect

International Journal of Mechanical Sciences

journal homepage: www.elsevier.com/locate/ijmecsci

Predicting elastic anisotropy of dual-phase steels based on crystal mechanics and microstructure

Aaron M. Cantara, Milovan Zecevic, Adnan Eghtesad, Camille M. Poulin, Marko Knezevic*

Department of Mechanical Engineering, University of New Hampshire, Durham, NH 03824, USA

ARTICLE INFO

Keywords:
Microstructures
Elastic material
Anisotropic material
Numerical algorithms
Dual-phase steel

ABSTRACT

This work utilizes mean-field self-consistent and full-field fast Fourier transform-based homogenizations to study the effective elastic behavior of several steels: three dual-phase (DP), DP 590, DP 980, and DP 1180, and one martensitic (MS), MS 1700. Crystallographic textures and phase fractions of these steels are characterized using electron microscopy along with electron-backscattered diffraction to initialize the models. A comprehensive set of Young's modulus and Poisson's ratio data, measured at the ambient temperature as a function of orientation with respect to the rolling direction for each steel sheet, is used to calibrate and validate the models. The calibration of the models enabled us to estimate the single crystal elastic constants for both the martensitic phase and ferrite, while calculating the orientation dependent effective properties. Half of the data was used in the calibration. Subsequent predictions of the orientation dependent effective elastic properties for the remaining data verified that the estimated single crystal properties are reliable. As the steels exhibit a different level of anisotropy in their effective behavior, good predictions allowed us to discuss the role of texture, grain structure, phase fraction and distribution on the effective properties. The results of this work represent a significant incentive to introduce elastic anisotropy in numerical tools for simulating metal forming processes of dual-phase steels, in particular those processes involving springback, using the texture informed crystal mechanics-based models to more accurately estimate the effective elastic properties required by such simulations.

1. Introduction

Simulations of manufacturing processes and mechanical designs involving polycrystalline metals are performed more accurately if the material constitutive behavior is modeled as anisotropic. The basic building block of a polycrystalline material, the single crystal referred to as a grain having a certain crystal lattice orientation, is known to exhibit anisotropic behavior [1,2]. Thermo-mechanical processing of polycrystalline aggregates generates a distribution of crystal lattice orientations, which is referred to as crystallographic texture [3]. Texture is not random but actually preferred depending on the directionality of active crystallographic deformation mechanisms, which accommodate shape change during shaping operations. A preferred distribution of crystal orientations can either enhance or suppress the anisotropy of effective properties. Interactions between individual grains of different crystal orientations exhibiting anisotropy in their properties under load creates inter-granular stress fields. The local mechanical fields are even more heterogeneous in multi-phase materials such as dual-phase (DP) steels containing a distribution of martensite and ferrite phases with contrasting mechanical characteristics.

The crystal elastic properties play the central role in governing the extent of backstress fields under load, or residual stress fields upon load removal [4]. A tensorial measure describing the resistance to stretch a crystal elastically in an anisotropic manner is referred to as elastic stiffness. Capturing the distribution of elastic backstress fields is especially important for modeling the material behavior during strain-path-changes [5]. Upon a strain-path-change, the material exhibits elastic unloading followed by a change in the yield stress from the one reached at the end of pre-straining, while the newly applied stress combines with the existing elastic backstress field [6,7]. After a metallic part is removed from a forming die, the field further evolves to a new equilibrium, which is accompanied with geometrical changes of the part referred to as springback. For example, upon completion of sheet metal forming, deep-drawn or stretch-drawn parts "spring back", affecting the dimensional accuracy of a finished part. The dimensional changes are directly dependent on the effective elastic properties of the sheet. Thus, the constitutive model used in predicting springback in metal forming should consider elastic anisotropy, as highlighted in [8,9]. Accurate predictions of springback are accentuated with the development of modern alloys for the transportation industry for vehicle light-weighting

---

* Corresponding author: Department of Mechanical Engineering, University of New Hampshire, 33 Academic Way, Kingsbury Hall, W119, Durham, NH 03824, USA.

E-mail address: marko.knezevic@unh.edu (M. Knezevic).

https://doi.org/10.1016/j.ijmecsci.2018.12.021
Received 11 November 2018; Received in revised form 7 December 2018; Accepted 11 December 2018

purposes, such as the advanced-high strength steels (AHSS), which exhibit high flow stress or aluminum and magnesium alloys, which exhibit low stiffness, both of which accentuate the magnitude of springback. Premier examples of AHSS are DP steels containing variable fractions of martensite vs. ferrite phases in their microstructure. This paper is concerned with the effective elastic behavior of DP steels based on the single crystal mechanics and microstructure.

Estimates of the effective elastic behavior of DP steels depend on microstructure and the accuracy of available single crystal constants for martensite and ferrite along with the homogenization procedure linking the crystal to the overall effective elastic response of the polycrystal. Published experimental measurements and theoretical estimates of single crystal elastic constants for martensitic and ferrite phases are rare, as they are difficult to measure and also difficult to theoretically calculate. Furthermore, the reported values vary substantially. Tables that summarize values based on a literature review are given in Appendix A. As is evident, while the elastic crystal stiffness coefficients of iron (Fe) have been reliably determined by many independent sources, the stiffness coefficients of ferrite and martensite have yet to be established with confidence.

We present estimates of the single crystal elastic coefficients for martensite and ferrite, based on the calibration and validation of mean-field self-consistent (SC) and full-field fast Fourier transform (FFT)-based homogenizations towards a comprehensive set of Young's modulus and Poisson's ratio data measured at the ambient temperature as a function of orientation with respect to the rolling direction (RD) for three DP steels, DP 590, DP 980, and DP 1180, and one martensitic (MS) steel, MS 1700. The effective elastic properties have been measured at 15° increments from the RD of the sheets. The specific models considered in the present work are the elasto-plastic SC (EPSC) [10–12] and the elasto-viscoplastic FFT (EVPFFT) [13,14] in which the strain is restricted to be elastic. While the former is much more computationally efficient, the latter is regarded as more accurate and can be used to validate the former. Texture and phase fractions of these steels are characterized using scanning electron microscopy (SEM) and electron-backscattered diffraction (EBSD) to initialize the models. Taking the characterized microstructure and the single crystal elastic constants as inputs, the models calculate the orientation dependent effective elastic behavior of the steels. The constants for martensite and ferrite are varied to fit the orientation dependent and microstructure sensitive effective response of DP 590 and MS 1700 using an optimization scheme and then verified by predicting the response of DP 980 and DP 1180. Thus, the effective property measurements along with the microstructural measurements are computationally linked to establish single crystal elastic constants for ferrite and martensite. As the steels exhibit a different level of anisotropy in their effective behavior, good predictions allowed us to discuss the role of texture, grain structure, phase fraction and distribution on the effective properties.

2. Modeling framework for predicting the anisotropic elastic response of polycrystals

This section summarizes homogenization approaches for calculating effective elastic properties and a procedure for obtaining the effective properties as a function of orientation with respect to sheet sample directions. In our notation, tensors are denoted by bold non-italic letters, while scalars and tensor components are italic and not bold.

The fourth rank crystal elastic stiffness tensor as a function of the crystal orientation can be calculated as

$$\begin{aligned}\mathbf{C}^c &= C^c_{ijkl} = g_{ip}g_{jq}g_{kr}g_{ls}[C_{12}\delta_{pq}\delta_{rs} + C_{44}(\delta_{ps}\delta_{qs} + \delta_{ps}\delta_{qr}) \\ &\quad + (C_{11} - C_{12} - 2C_{44}) \textstyle\sum_{t=1}^{3} \delta_{pt}\delta_{qt}\delta_{rt}\delta_{st}],\end{aligned} \tag{1}$$

where δ_{ij} represents the Kronecker delta symbol, C_{12}, C_{12}, and C_{44} are the single crystal elastic stiffness constants for a cubic crystal, and g_{ij} are components of an orthogonal coordinate transformation matrix relating a crystal to a sample frame as

$$\mathbf{g} = \begin{bmatrix} \cos\phi_1\cos\phi_2 - \sin\phi_1\cos\Phi\sin\phi_2 & -\cos\phi_1\sin\phi_2 - \sin\phi_1\cos\Phi\sin\phi_2 & \sin\phi_1\sin\Phi \\ \sin\phi_1\cos\phi_2 + \cos\phi_1\cos\Phi\sin\phi_2 & -\sin\phi_1\sin\phi_2 + \cos\phi_1\cos\Phi\cos\phi_2 & -\cos\phi_1\sin\Phi \\ \sin\Phi\sin\phi_2 & \sin\Phi\cos\phi_2 & \cos\Phi \end{bmatrix} \tag{2}$$

The first-order lower (Reuss) and upper (Voigt) bounds for the effective elastic stiffness tensor have been well established in the literature [15–22]. The bounds for the diagonal components are

$$\left(\langle\mathbf{S}^c\rangle^{-1}\right)_{ijij} \le C^*_{ijij} \le \left\langle C^c_{ijij}\right\rangle \tag{3}$$

while those for the off-diagonal components are

$$\begin{aligned}&\max\left(\left\langle C^c_{ijkl}\right\rangle, (\langle\mathbf{S}^c\rangle^{-1})_{ijkl}\right) - \sqrt{\Delta_{ijij}\Delta_{klkl}} \\ &\quad\le C^*_{ijkl} \le \min\left(\left\langle C^c_{ijkl}\right\rangle, (\langle\mathbf{S}^c\rangle^{-1})_{ijkl}\right) + \sqrt{\Delta_{ijij}\Delta_{klkl}},\end{aligned} \tag{4a}$$

$$\Delta_{ijkl} = \left\langle C^c_{ijkl}\right\rangle - (\langle\mathbf{S}^c\rangle^{-1})_{ijkl}. \tag{4b}$$

Here, no implicit summation on repeated indices is used.[1] The angle brackets ⟨ ⟩ are used to denote the volume averaged value over constituent crystals in a polycrystal. $\mathbf{S}^c = (\mathbf{C}^c)^{-1}$ is the single crystal compliance tensor.

The constitutive relation for linear elasticity that holds for anisotropic materials expressed in terms of matrices in the Voigt form [23] is

$$\begin{pmatrix}\Sigma_{11}\\ \Sigma_{22}\\ \Sigma_{33}\\ \Sigma_{23}\\ \Sigma_{31}\\ \Sigma_{12}\end{pmatrix} = \begin{pmatrix} C^*_{1111} & C^*_{1122} & C^*_{1133} & C^*_{1123} & C^*_{1131} & C^*_{1112}\\ C^*_{2211} & C^*_{2222} & C^*_{2233} & C^*_{2223} & C^*_{2231} & C^*_{2221}\\ C^*_{3311} & C^*_{3322} & C^*_{3333} & C^*_{3323} & C^*_{3331} & C^*_{3312}\\ C^*_{3211} & C^*_{3222} & C^*_{2333} & C^*_{2323} & C^*_{2331} & C^*_{2312}\\ C^*_{3111} & C^*_{3122} & C^*_{3133} & C^*_{3132} & C^*_{3131} & C^*_{3112}\\ C^*_{1211} & C^*_{1222} & C^*_{1233} & C^*_{1223} & C^*_{1231} & C^*_{1212} \end{pmatrix} \begin{pmatrix}E_{11}\\ E_{22}\\ E_{33}\\ 2E_{23}\\ 2E_{31}\\ 2E_{12}\end{pmatrix} \tag{5}$$

In this reducing order notation, the macroscopic Cauchy stress tensor, $\mathbf{\Sigma}$, and macroscopic strain tensor, $\mathbf{E}$, are expressed as column vectors and the effective stiffness tensor is expressed as a symmetric matrix. The inverse relation is

$$\begin{pmatrix}E_{11}\\ E_{22}\\ E_{33}\\ 2E_{23}\\ 2E_{31}\\ 2E_{12}\end{pmatrix} = \begin{pmatrix} S^*_{1111} & S^*_{1122} & S^*_{1133} & 2S^*_{1123} & 2S^*_{1131} & 2S^*_{1112}\\ S^*_{2211} & S^*_{2222} & S^*_{2233} & 2S^*_{2223} & 2S^*_{2231} & 2S^*_{2221}\\ S^*_{3311} & S^*_{3322} & S^*_{3333} & 2S^*_{3323} & 2S^*_{3331} & 2S^*_{3312}\\ 2S^*_{3211} & 2S^*_{3222} & 2S^*_{2333} & 4S^*_{2323} & 4S^*_{2331} & 4S^*_{2312}\\ 2S^*_{3111} & 2S^*_{3122} & 2S^*_{3133} & 4S^*_{3132} & 4S^*_{3131} & 4S^*_{3112}\\ 2S^*_{1211} & 2S^*_{1222} & 2S^*_{1233} & 4S^*_{1223} & 4S^*_{1231} & 4S^*_{1212} \end{pmatrix} \begin{pmatrix}\Sigma_{11}\\ \Sigma_{22}\\ \Sigma_{33}\\ \Sigma_{23}\\ \Sigma_{13}\\ \Sigma_{12}\end{pmatrix} \tag{6}$$

2.1. Effective properties

The effective properties relating $\mathbf{\Sigma}$ and $\mathbf{E}$ can be estimated with the knowledge of local stress and strain fields in the polycrystal. The macroscopic Cauchy stress tensor, $\mathbf{\Sigma}$, and macroscopic strain tensor, $\mathbf{E}$, are

$$\mathbf{\Sigma} = < \boldsymbol{\sigma}(\mathbf{x}) >, \tag{7a}$$

$$\mathbf{E} = < \boldsymbol{\varepsilon}(\mathbf{x}) >, \tag{7b}$$

where $\boldsymbol{\sigma}(\mathbf{x})$ is a local stress tensor, $\boldsymbol{\varepsilon}(\mathbf{x})$ is a local strain tensor, and $\mathbf{x}$ is a spatial coordinate, which belongs to a crystal c. The superscript c is dropped when the spatial coordinate $\mathbf{x}$ is indicated. The general framework for calculating the local stress and strain fields, entering Eqs. (7a) and (7b), in a heterogeneous polycrystal undergoing a prescribed macroscopic strain tensor is outlined next [24–26]. The local constitutive relation is

$$\boldsymbol{\sigma}(\mathbf{x}) = \mathbf{C}(\mathbf{x})\boldsymbol{\varepsilon}(\mathbf{x}). \tag{8}$$

---

[1] The Einstein indicial notation of implicit summation on repeated indices is employed in this paper, except when explicitly noted otherwise.

where $\mathbf{C}(\mathbf{x})$ is the local elastic stiffness at $\mathbf{x}$ in a grain c. The local elastic stiffness can be expressed in terms of an elastic stiffness of a fictitious homogenous reference medium as

$$\mathbf{C}(\mathbf{x}) = \mathbf{C}^0 + \delta\mathbf{C}(\mathbf{x}), \tag{9}$$

where $\mathbf{C}^0$ is the elastic stiffness of the homogenous reference medium and $\delta\mathbf{C}(\mathbf{x})$ is the deviation of the local elastic stiffness at $\mathbf{x}$ from elastic stiffness of the homogenous reference medium. The equilibrium statement in the absence of a body force can be written using Eqs. (8) and (9)

$$C^0_{ijkl}u_{k,lj}(\mathbf{x}) + \left(\delta C_{ijkl}(\mathbf{x})u_{k,l}(\mathbf{x})\right)_{,j} = 0, \tag{10}$$

where $u_k(\mathbf{x})$ is the local displacement vector and the product of $\delta C_{ijkl}(\mathbf{x})$ and $u_{k,l}(\mathbf{x})$ is known as the polarization field, ϕ_{ij}. Eq. (10) can be viewed as the equilibrium statement for the homogenous reference medium with a prescribed distribution of the fictitious body force, $\phi_{ij,j}$. Using the Green function method allows transformation of Eq. (10) into an integral equation

$$\tilde{u}_{k,l}(\mathbf{x}) = \int_{R^3} G_{ki,jl}\left(\mathbf{x}-\mathbf{x}'\right)\phi_{ij}\left(\mathbf{x}'\right)d\mathbf{x}', \tag{11}$$

where $\tilde{u}_{k,l}(\mathbf{x})$ is the local displacement gradient fluctuation, $G_{ki}(\mathbf{x}-\mathbf{x}')$ is Green's function for the infinite homogenous reference medium, and the integral is generically over the entire three-dimensional space, R^3. Eqs. (5), (7a), and (7b) together with the solution of the integral in Eq. (11) facilitate solving for the effective properties of the polycrystal [26]. In this work, we will use two approaches to solve for the integral in Eq. (11) in order to estimate homogenized effective stiffness for polycrystals: (1) the mean-field SC approach and (2) the full-field FFT-based approach.

2.1.1. Mean-field self-consistent homogenization for estimating effective elastic properties

This section summarizes the solution to Eq. (11) using the SC approach, which is valid for granular media i.e. polycrystals. The SC approach facilitates the evaluation of the effective elastic stiffness in a computationally efficient manner. The underlying assumptions can be found elsewhere e.g. [26,27], while the actual SC scheme used here is from [10,28].

Each crystal is represented as an ellipsoidal heterogeneity within the infinite homogenous reference medium under applied displacement. Elastic stiffness of the reference homogenous medium is set equal to the unknown effective elastic stiffness i.e. $C^0_{ijkl} = C^*_{ijkl}$, while the elastic stiffness of each crystal, C^c_{ijkl}, is assumed to be uniform within the crystal volume c. The problem can be reduced to Eshelby's inclusion problem [27] with an appropriate choice of eigenstrain, meaning that the strain and stress within the heterogeneity are constant. The polarization tensor, $\phi_{ij}(\mathbf{x}')$, is zero outside the inclusion volume and constant within the inclusion i.e. fictitious body force is only present in the inclusion volume. Eq. (11) can be integrated over the volume of the inclusion to calculate the average displacement gradient deviation in the inclusion [26]

$$\tilde{u}^c_{k,l} = \frac{1}{V_c}\int_{V_c}\int_{V_c} G_{ki,jl}\left(\mathbf{x}-\mathbf{x}'\right)d\mathbf{x}'d\mathbf{x}\left(C^c_{ijmn} - C^*_{ijmn}\right)u^c_{m,n}, \tag{12}$$

where $u^c_{m,n}$ is the average displacement gradient in the inclusion i.e. crystal. Defining the strain in the inclusion as the symmetric part of the displacement gradient, $u^c_{k,l}$, and invoking the minor symmetry of the elastic stiffness, gives

$$\varepsilon^c_{kl} = E_{kl} + \frac{1}{V_c}\int_{V_c}\int_{V_c}\frac{1}{2}\left[G_{ki,jl}\left(\mathbf{x}-\mathbf{x}'\right) + G_{li,jk}\left(\mathbf{x}-\mathbf{x}'\right)\right]d\mathbf{x}'d\mathbf{x}\left(C^c_{ijmn} - C^*_{ijmn}\right)\varepsilon^c_{mn} \tag{13}$$

where E_{kl} is the macroscopically imposed strain tensor i.e. the strain in the homogenous reference medium. The integral $\int_{V_c}\frac{1}{2}[G_{ki,jl}(\mathbf{x}-\mathbf{x}') + G_{li,jk}(\mathbf{x}-\mathbf{x}')]d\mathbf{x}'$ is uniform in the volume of the inclusion, meaning that the strain inside the inclusion is also uniform. The symmetric Eshelby tensor is defined as $S^c_{klpq} = \int_{V_c}\frac{1}{2}[G_{ki,jl}(\mathbf{x}-\mathbf{x}') + G_{li,jk}(\mathbf{x}-\mathbf{x}')]d\mathbf{x}'C^*_{ijpq}$ [29]. Then, the strain in the inclusion is

$$\varepsilon^c_{kl} = \left[I_{klmn} + S^c_{klpq}\left(C^*_{pqij}\right)^{-1}\left(C^c_{ijmn} - C^*_{ijmn}\right)\right]^{-1}E_{mn} = A^c_{klmn}E_{mn} \tag{14}$$

where I_{ijkl} is the fourth rank identity tensor, A^c_{ijkl} is a localization (or concentration) tensor. Using Eqs. (5), 7a), (7b) and (14), the effective stiffness is

$$C^*_{ijkl} = < C^c_{ijpq}A^c_{pqmn} > < A^c_{mnkl} >^{-1}. \tag{15}$$

Since the localization tensor, A^c_{pqmn}, is a function of the effective stiffness, C^*_{ijkl}, Eq. (15) is solved numerically using the fixed point iterations [10].

2.1.2. Full-field FFT homogenization for estimating effective elastic properties

Effective properties of a microstructural cell embedding crystal properties can be solved using full-field approaches like finite elements with sub-grain mesh resolution [30–36] or a Green's function-based method, which relies on the efficient FFT algorithm to solve the convolution integral representing stress equilibrium under strain compatibility constraint over a voxel-based microstructural cell. The later approach is utilized here as a more accurate but less computationally efficient alternative to the SC homogenization.

In this formulation, Eq. (11) is solved in Fourier space, which is then followed by the inverse transform to obtain the strain as

$$\varepsilon_{ij}(\mathbf{x}) = E_{ij} + FT^{-1}\left(sym\left(\hat{\Gamma}^0_{ijkl}(\mathbf{k})\right)\hat{\phi}_{kl}(\mathbf{k})\right), \tag{16}$$

where the symbols "^" and FT^{-1} indicate direct and inverse Fourier transforms, respectively, while *sym* indicates the symmetric portion and $\mathbf{k}$ is a point (frequency) in Fourier Space. The fourth order tensor $\hat{\Gamma}^0_{ijkl}(\mathbf{k})$ is

$$\hat{\Gamma}^0_{ijkl}(\mathbf{k}) = -k_jk_l\hat{G}_{ik}(\mathbf{k});\ \hat{G}_{ik}(\mathbf{k}) = [C_{kjil}k_lk_j]^{-1}. \tag{17}$$

Guessing the stress, ${\lambda_{ij}}^{(i)}$, and corresponding elastic strain, ${e_{ij}}^{(i)}$, at an iteration (i), the polarization field is

$$\phi_{ij}{}^{(i)}(\mathbf{x}) = \lambda_{ij}{}^{(i)}(\mathbf{x}) - C^0{}_{ijkl}\,e_{kl}{}^{(i)}(\mathbf{x}). \tag{18}$$

The new guess for strain field at $(i+1)$ is then

$$e_{ij}{}^{(i+1)}(\mathbf{x}) = E_{ij} + FT^{-1}\left(sym\left(\hat{\Gamma}^0_{ijkl}(\mathbf{k})\right)\hat{\phi}^{(i)}_{kl}(\mathbf{k})\right). \tag{19}$$

The stress field is iteratively solved using a suitably defined residual

$$R_k(\boldsymbol{\sigma}^{(i+1)}) = \sigma_k{}^{(i+1)} + C_{kl}{}^0\varepsilon_l{}^{(i+1)}(\boldsymbol{\sigma}^{(i+1)}) - \lambda_k{}^{(i)} - C_{kl}{}^0e_l{}^{(i+1)} = 0. \tag{20}$$

In Eq. (20), the Voigt form is employed as

$$\begin{aligned} &\sigma_{ij} \rightarrow \sigma_k, && k = 1..6,\\ &C_{ijkl} \rightarrow C_{mn} && m,n = 1..6. \end{aligned} \tag{21}$$

The solution is obtained using the Newton's solution procedure

$$\sigma_k{}^{(i+1,j+1)} = \sigma_k{}^{(i+1,j)} - \left(\left.\frac{\partial R_k}{\partial\sigma_l}\right|_{\boldsymbol{\sigma}^{(i+1,j)}}\right)^{-1}R_l(\boldsymbol{\sigma}^{(i+1,j)}), \tag{22}$$

where j enumerates the iterations for stress. The convergence is controlled by

$$\left.\frac{\partial R_k}{\partial\sigma_l}\right|_{\boldsymbol{\sigma}^{(i+1,j)}} = \delta_{kl} + C_{kq}{}^0C_{ql}{}^{-1} \tag{23}$$

The stress solution is used as a next guess in Eq. (18) until convergence is achieved in which $\boldsymbol{\sigma}$ approaches λ and ε approaches $\mathbf{e}$.

Upon the convergence, a homogenization over voxels of the microstructural cell is performed as follows

$$\begin{aligned} \Sigma_{ij} &= \frac{\sum_{X,Y,Z}\left(\sigma_{ij}(\mathbf{x})\right)}{N^3};\ N = \#\ of\ voxels\ in\ X,Y,Z,\\ E_{ij} &= \frac{\sum_{X,Y,Z}\left(\varepsilon_{ij}(\mathbf{x})\right)}{N^3}. \end{aligned} \tag{24}$$

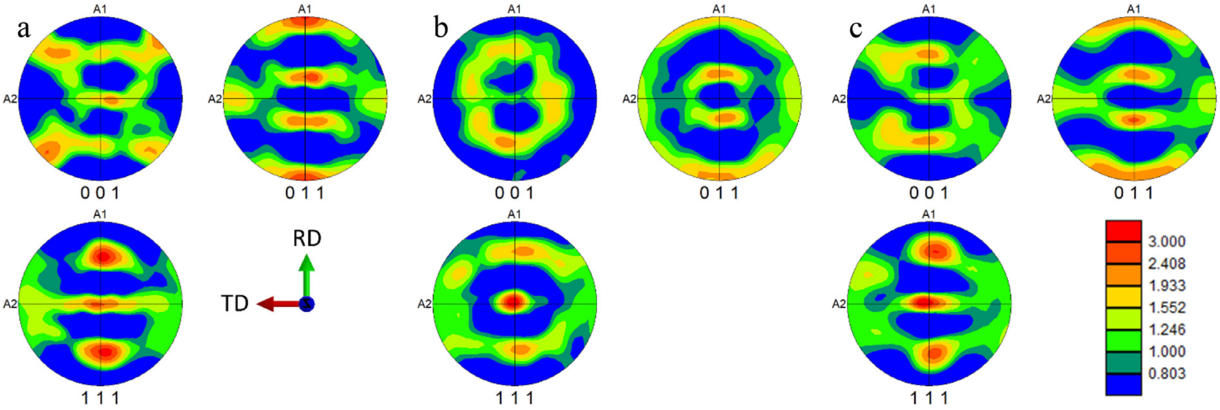

Fig. 1. Stereographic pole figures showing initial texture of (a) DP 590, (b) DP 980, and (c) DP 1180 steel sheets.

Since an equivalent expression to Eq. (15) for the full-field FFT homogenization is not readily available, an alternative procedure is used to obtain the effective macroscopic stiffness for a given microstructural cell. The procedure involves several steps:

i Set six simulations such that

$$E_{ij}^{(1)}=\begin{bmatrix}1.0&0.0&0.0\\0.0&0.0&0.0\\0.0&0.0&0.0\end{bmatrix},\ E_{ij}^{(2)}=\begin{bmatrix}0.0&0.0&0.0\\0.0&1.0&0.0\\0.0&0.0&0.0\end{bmatrix},\ E_{ij}^{(3)}=\begin{bmatrix}0.0&0.0&0.0\\0.0&0.0&0.0\\0.0&0.0&1.0\end{bmatrix},$$
$$E_{ij}^{(4)}=\begin{bmatrix}0.0&0.0&0.0\\0.0&0.0&0.5\\0.0&0.5&0.0\end{bmatrix},\ E_{ij}^{(5)}=\begin{bmatrix}0.0&0.0&0.5\\0.0&0.0&0.0\\0.5&0.0&0.0\end{bmatrix},\ E_{ij}^{(6)}=\begin{bmatrix}0.0&0.5&0.0\\0.5&0.0&0.0\\0.0&0.0&0.0\end{bmatrix}. \tag{25}$$

ii Run each simulation to obtain the individual components of elastic stiffness

$$\begin{aligned}
\Sigma_{ij}^{(1)}&=C_{ijkl}^{*}E_{kl}^{(1)}=C^{eff}{}_{ij11}\,E_{11}^{(1)}=C_{ij11}^{*}\\
\Sigma_{ij}^{(2)}&=C_{ijkl}^{*}E_{kl}^{(2)}=C_{ij22}^{*}\,E_{22}^{(2)}=C_{ij22}^{*}\\
\Sigma_{ij}^{(3)}&=C_{ijkl}^{*}E_{kl}^{(3)}=C_{ij33}^{*}\,E_{33}^{(3)}=C^{eff}{}_{ij33}\\
\Sigma_{ij}^{(4)}&=C_{ijkl}^{*}E_{kl}^{(4)}=C_{ij23}^{*}E_{23}^{(4)}+C_{ij32}^{*}E_{32}^{(4)}=\frac{1}{2}\left(C_{ij23}^{*}+C_{ij32}^{*}\right)=C_{ij23}^{*}\\
\Sigma_{ij}^{(5)}&=C_{ijkl}^{*}E_{kl}^{(5)}=C_{ij13}^{*}E_{13}^{(5)}+C_{ij31}^{*}E_{31}^{(5)}=\frac{1}{2}\left(C_{ij13}^{*}+C_{ij31}^{*}\right)=C_{ij13}^{*}\\
\Sigma_{ij}^{(6)}&=C_{ijkl}^{*}E_{kl}^{(6)}=C_{ij12}^{*}E_{12}^{(6)}+C_{ij21}^{*}E_{21}^{(6)}=\frac{1}{2}\left(C_{ij12}^{*}+C_{ij21}^{*}\right)=C_{ij12}^{*}\\
ij&=11,22,33,23,13,12.
\end{aligned} \tag{26}$$

iii Form the effective elastic stiffness tensor from the components obtained in Eq. (26).

2.2. *Obtaining Young's modulus, Poisson's ratio, and shear modulus from an effective elastic tensor*

The effective elastic stiffness and compliance tensors as outputs from the homogenization approaches are defined with respect to the rolling direction (RD) as $\mathbf{e}_1$, the transverse direction (TD) as $\mathbf{e}_2$, and the normal direction (ND) as $\mathbf{e}_3$ of the steel sheets: $\mathbf{C}^{*}=C_{ijkl}^{*}\mathbf{e}_i\otimes\mathbf{e}_j\otimes\mathbf{e}_k\otimes\mathbf{e}_l$ and $\mathbf{S}^{*}=S_{ijkl}^{*}\mathbf{e}_i\otimes\mathbf{e}_j\otimes\mathbf{e}_k\otimes\mathbf{e}_l$, respectively. Young's modulus along $\mathbf{e}_1$ can be determined by examining the case of a simple tension in $\mathbf{e}_1$. Eq. (6) reduces to $E_{11}=S_{1111}^{*}\Sigma_{11}$ which can be rearranged into

$$\text{Young's Modulus}=\frac{\Sigma_{11}}{E_{11}}=\frac{1}{S_{1111}^{*}}. \tag{27}$$

Similarly, Poisson's ratio, ν_{12} can be determined using the simple tension case as

$$\text{Poisson's Ratio}=-\frac{E_{22}}{E_{11}}=-\frac{S_{2211}^{*}}{S_{1111}^{*}} \tag{28}$$

Finally, shear modulus, μ_{12}, is

$$\text{Shear Modulus}=\frac{1}{4S_{1212}^{*}} \tag{29}$$

The stiffness tensor, $\mathbf{C}^{*}$, given with respect to the reference frame of the sheet, can be transformed using the coordinate transformation law into another frame $\mathbf{e}_i'$. The direction cosines transformation matrix for change of basis is a dot product between vectors representing the reference frame of the sheet and the transformed frame, $Q_{ij}=\mathbf{e}_i\cdot\mathbf{e}_j'$.

$$C_{ijkl}^{*'}=Q_{ip}Q_{jq}Q_{kr}Q_{ls}C_{pqrs}^{*} \tag{30}$$

The transformation matrix, Q_{ij}, can be conveniently established using two angles, where one rotates about $\mathbf{e}_3$ (i.e. ϕ_1 in Eq. (2)) to obtain $C_{ijkl}^{*'}$ along any in-plane sheet orientation and another rotates about $\mathbf{e}_1$ (i.e. Φ in Eq. (2)) to obtain $C_{ijkl}^{*'}$ along any orientation in three-dimensional (3D) space. The transformed stiffness matrix $C_{ijkl}^{*'}$ is then inverted to get $S_{ijkl}^{*'}$, which is then used to determined Young's modulus and Poisson's ratio along selected in-plane sheet orientation using $\frac{1}{S_{1111}^{*'}}$ and $-\frac{S_{2211}^{*'}}{S_{1111}^{*'}}$, respectively.

3. Results

3.1. *Microstructure*

The materials investigated in this study are commercial steel sheets received from US Steel. The studied steels are typical of auto-body/structure applications. We begin by presenting texture for the sheets as characterized using EBSD. Fig. 1 shows stereographic pole figures visualizing the texture for the ferrite phase in DP 590, DP 980, and DP 1180. The data for DP 590 was taken from [37]. The EBSD scans were run over a very large area for each steel to obtain statistically significant data. The texture evolution in the sheets resembles classically reported orthotropic rolled texture for body-centered cubic (BCC) materials, where a majority of the grains are concentrated around the γ-fiber and a portion of the α-fiber [3,38–45]. We have attempted to separate the texture of the martensitic phase in each steel and obtained these to be weak (i.e. approximately random). While the measured EBSD scans consisted of over a million index-able points with high confidence index for ferrite for each sheet, textures used in the simulations were compacted to 1,000 weighted orientations using the recently developed procedures [46,47]. Sum of the weights corresponded to the fraction of ferrite for each steel. Texture used in the simulation for the martensitic phase was also represented by 1000 orientations, which were approximated as uniform random. Likewise, for ferrite, the sum of the weights of orientations for the martensite phase corresponded to the measured fraction of martensite for each steel. The phase fractions were measured using a combination of EBSD and SEM imaging, where the latter method

Table 1
Measured fraction of martensitic phase per steel.

Steel	DP 590	DP 980	DP 1180	MS 1700
Fraction	0.077	0.33	0.42	0.90

was used to verify the former method. Since regions of martensite appear as dark regions in image quality (IQ) maps [37,48], the volume fraction of martensite was determined using a threshold procedure from IQ maps of high resolution. The obtained estimates were verified by analyzing many SEM images. Table 1 presents the measured fraction of martensite for each steel.

3.2. Calibration

To study elastic anisotropy of dual-phase steels as a function of their microstructural features, we first employ the SC homogenization to estimate the effective elastic properties. The microstructural variables considered by the SC homogenization are restricted to texture and phase fraction. The steels used in this study have similar texture but contain an increasing volume fraction of martensite within a ferrite matrix (Table 1). The content of martensite is likely the main microstructural feature governing the difference in their elastic behavior. To begin, texture and phase fraction of DP 590 as a predominantly ferritic streel and MS 1700 as a predominantly martensitic steel are used to appropriately initialize the SC modeling framework put together to extract the single crystal constants. As a consequence of cubic crystal symmetry, BCC for ferrite and body-centered tetragonal for martensite require only three crystal stiffness coefficients, C_{11}, C_{12}, and C_{44} to define their single-crystal stiffness tensors. These three crystal constants per phase are a user defined input in the SC model, in addition to the input in terms of the phase fractions and texture per phase. The objective is to determine the crystal stiffness coefficients of ferrite and martensite while calculating the orientation dependent effective data for Young's modulus and Poisson's ratio with respect to RD for the two sheets. The data is taken from [49]. Additionally, the data for the shear modulus was available for MS 1700 [50]. We set a direct-search optimization algorithm to find the optimal constants while matching the experimental data with the output of the SC homogenization.

Since the elastic stiffness coefficients of ferrite are expected to be similar to those of Fe, we used them as the initial guess. The elastic crystal stiffness coefficients of Fe have been reliably determined by many independent sources (Appendix A). The two-tier direct-search optimization algorithm was set to minimize the error between the calculated and mean of the measured effective values for two steels in seven directions (RD = 0°, 15°, 30°, 45°, 60°, 75°, and TD = 90°) to determine the crystal elastic stiffness coefficients for ferrite and martensite. For every combination of the constants, the effective stiffness tensors are calculated for the two steels using the SC homogenization model. The two effective stiffness tensors are then passed to the program for performing the change of basis and obtaining Young's modulus, Poisson's ratio, and shear modulus for two steels in every direction. The first stage of the program considered only the experimental data for Poisson's ratio and varied all six coefficients at once. The second stage of the program kept the anisotropy ratio constant and varied only the overall magnitude of the constants to minimize the error for Young's Modulus. Thus, both the level of anisotropy and the magnitude of the constants were adjusted. The optimization scheme attempted to increase and decrease each crystal constant by a predetermined step size and the combination with the lowest error from the experimental data was used as the new initial value. This process continued until no change in the new initial constant values from the old values occurred.

Fig. 2 shows the comparison between measured and calculated variation of effective Young's modulus and Poisson's ratio with the in-plane

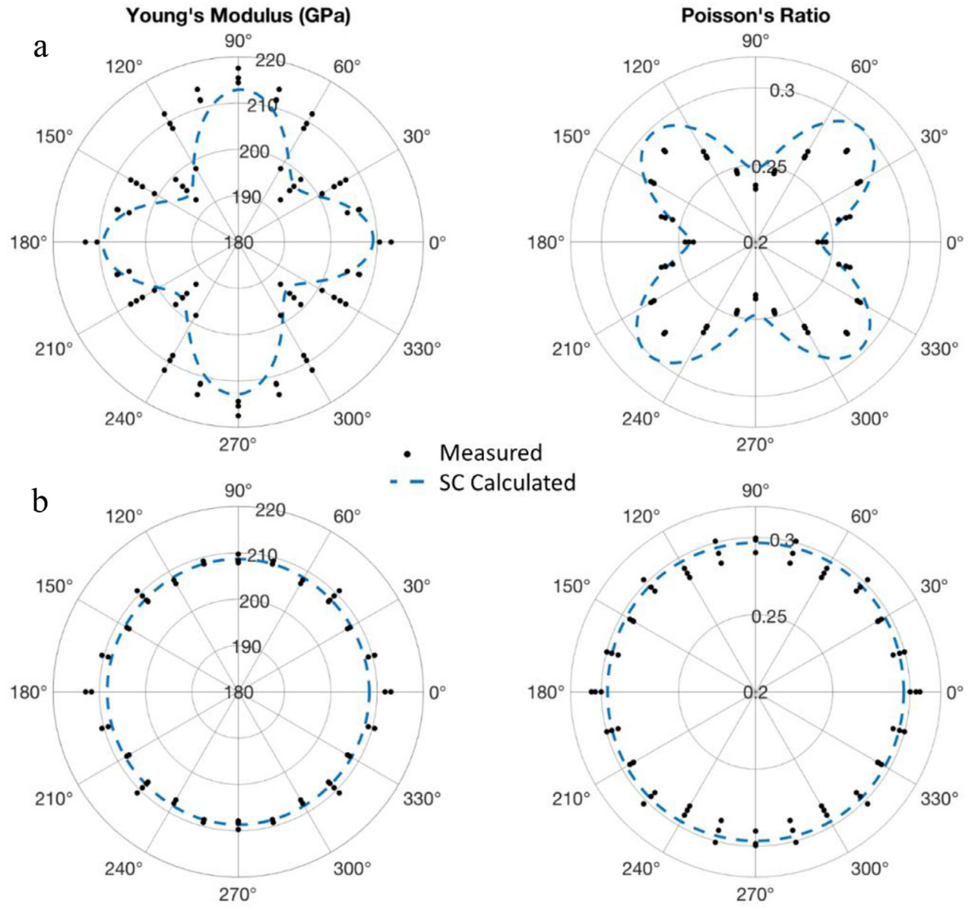

Fig. 2. Comparison of measured [49] and calculated variation of effective Young's modulus and Poisson's ratio with the in-plane sheet orientation: (a) DP 590 and (b) MS 1700. The angle starts from the rolling direction (i.e. 0° = RD). The calculations are performed using the mean-field self-consistent homogenization method.

Table 2
Comparison of measured [50] and calculated in-plane shear modulus (μ_{12}).

	MS 1700 (GPa)
Measured	78.0
SC Calculated	79.28

Table 3
Single crystal elastic stiffness values in GPa for ferrite and martensite estimated in this work.

	C_{11}	C_{12}	C_{44}
Ferrite	218.37	113.31	105.34
Martensite	282.31	116.19	78.57

sheet orientation for the two steels based on the optimized single crystal constants. Table 2 compares measured and calculated in-plane shear modulus. As is evident, the agreement is reasonably good suggesting that the calibrated single crystal constants should be reliable.

Table 3 presents the established single crystal values for both ferrite and martensite. Fig. 3 illustrates the dependence of Young's modulus for ferrite and martensite on orientation in 3D. These diagrams illustrate the level of anisotropy of single crystals. The behavior of ferrite is such that [100], [010], and [001] directions are softer, while the [111], $[1\bar{1}1]$, and $[11\bar{1}]$ directions are stiffer. Interestingly, for martensite, the opposite occurs but the anisotropy of Young's modulus is small. The coordinate axes correspond to slightly stiffer directions. Effective elastic behavior of polycrystalline DP steels is governed essentially by superposition of these two crystal diagrams weighted by their texture and phase fractions.

3.3. Verification using the full-field estimates

In order to verify the estimates of the single crystal constants and evaluate the sensitivity of the effective stiffness properties on microstructure, we designed several simulation setups for the full-field FFT solver to estimate the elastic stiffness of DP 590. Here, the role of grain, phase, and misorientation distributions as full-field microstructural features in governing the effective elastic properties can be assessed, in addition to phase fractions and texture as mean-field microstructural features. To this end, three synthetic microstructures with different grain strictures are generated using the DREAM3D software package [51]. The grain structure is based on the EBSD scans [37], ensuring the ratio between smaller martensite grains surrounded by the larger ferrite crystals and the volume fraction of the phases. Furthermore, the texture is shuffled three times using the “jumble orientations” function in DREAM3D to further vary the inter-granular misorientation distribution per microstructure realization. Numerical setups in terms of the 3D voxel-based microstructural cells and texture shuffles in each are shown in Fig. 4. Every microstructural cell consist of 128^3 voxels embedding 3,592 ferrite grains and 270 martensite grains. The measured texture was loaded in DREAM3D and assigned to ferrite, while a uniform random texture is assigned to martensite. The two categories of grains are designed as equiaxed and of similar volume per phase in each microstructural cell. Thus, texture and phase fractions were nearly the same in every microstructural realization as shuffles had minimal effect on the change in texture.

Fig. 5 shows the comparison of measured and calculated variation of effective Young's modulus and Poisson's ratio with the in-plane sheet orientation for DP 590 based on the full field calculations. The figure also shows the comparison between the SC estimates and the average of

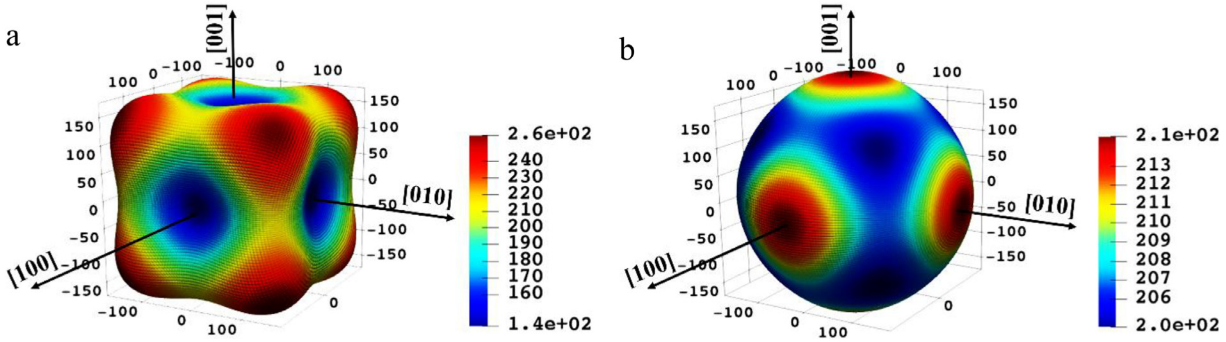

Fig. 3. Contour plots showing anisotropy of Young's modulus with orientation for single crystalline (a) ferrite phase and (b) martensitic phase.

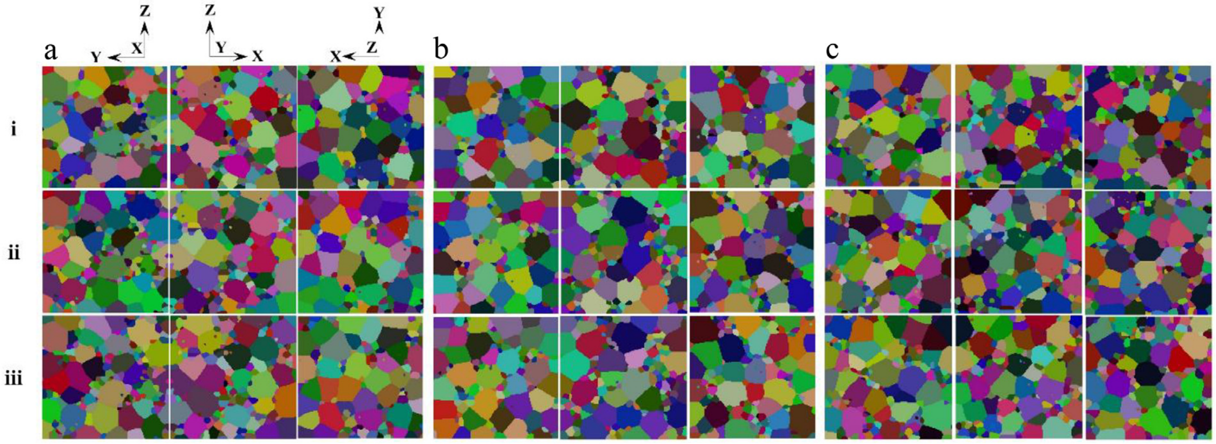

Fig. 4. Front, side, and top views of 3D voxel-based microstructural cells generated in DREAM.3D to synthetically represent grain structure of DP 590: (a) microstructural cell #, 1 (b) microstructural cell #2, (c) microstructural cell #3, (i) texture shuffle #1, (ii) texture shuffle #2, (iii) texture shuffle #3. The colors represent different grains. These numerical setups are used in the EVPFFT simulations of the effective elastic properties for DP 590.

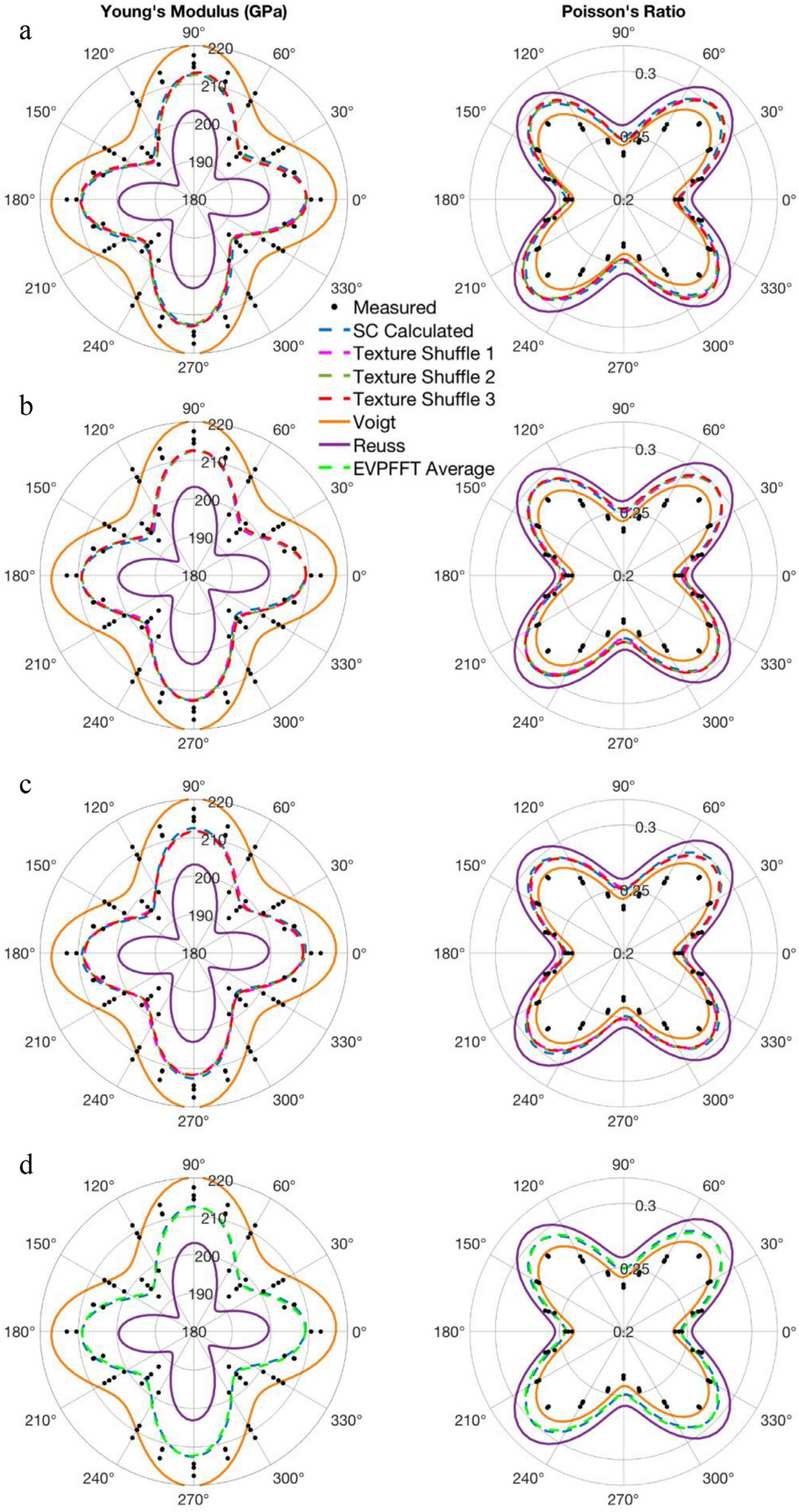

Fig. 5. Comparison of measured and calculated variation of effective Young's modulus and Poisson's ratio with the in-plane sheet orientation for DP 590. The angle starts from the rolling direction (i.e. 0° = RD). The calculations of the effective properties are performed using the full-field EVPFFT homogenization method based on (a) microstructural cell #1 (b) microstructural cell #2, (c) microstructural cell #3 with three texture shuffles in each. (d) Comparison between the SC and the average of the full-field FFT predictions. The property bounds are also plotted.

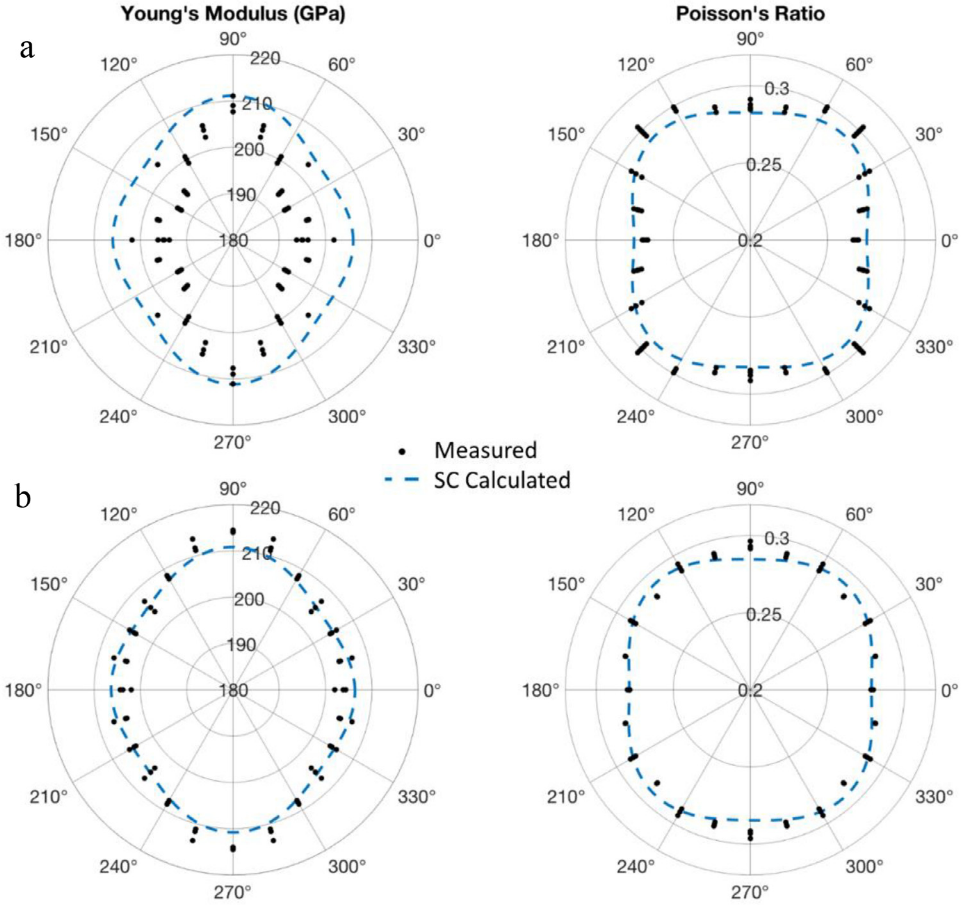

Fig. 6. Comparison of measured [49] and predicted variation of effective Young's modulus and Poisson's ratio with the in-plane sheet orientation: (a) DP 980 and (b) DP 1180. The angle starts from the rolling direction (i.e. 0° = RD). The calculations are performed using the mean-field self-consistent homogenization method.

the full-field FFT predictions. Additionally, the property bounds are plotted. First, it is observed that the effective values are within the bounds. Next, the effective elastic stiffness estimated using the full-field FFT solver and the SC approach are very similar, validating the single crystal elastic stiffness constants for both phases. Finally, the good agreement between the SC and FFT-based estimates suggests that texture and phase fractions play the major role in governing the effective elastic behavior, while grain, phase, and misorientation distributions are secondary. Although the grains of the martensite are much different than grains of the ferrite, the morphology effects still seem secondary.

4. Discussion

This work utilized the single crystal mechanics, homogenization theories, sets of microstructural characterization data, and sets of orientation dependent Young's modulus and Poisson's ratio data to reliably determine the single crystal elastic stiffness constants for ferrite and martensite. Two steels were suitably selected to facilitate the accurate determination of the constants per phase, one containing over 90% of ferrite (DP 590) and another containing up to 90% of martensite (MS 1700). Crystallographic texture and phase fractions have been characterized using EBSD and SEM. Taking texture and phase fractions as input into the model, the effective elastic behavior of two steels was modelled using the SC homogenization while calibrating the constants by matching the measured anisotropy. To this end, an optimization algorithm was developed to search for the optimal constant. The optimal constants were then successfully used within the full-field FFT model to verify the elasticity response of DP 590.

To further verify the established values, we simulate the orientation dependent Young's modulus and Poisson's ratio for DP 980 and DP 1180 using the SC approach. These calculations are regarded as predictions since the same set of single crystal constants for ferrite and martensite (Table 3) are used. The initial textures shown in Fig. 1 were used to initialize the ferrite phase per steel used in the SC model. Comparison of measured [49] and predicted variation of the effective properties with the in-plane sheet orientation is given in Fig. 6. Furthermore, Table 4 shows the predicted values of the shear modulus for both steels. Considering the predicted magnate of the effective properties and the shape of the curves, we regard these predictions as reasonably good. Appendix B presents values of the elastic stiffness tension components for the four studied steels.

Table 4
Comparison of measured [50] and predicted in-plane shear modulus (μ_{12}).

	DP 980 (GPa)	DP 1180 (GPa)
Measured	78.1	75.0
SC Predicted	79.40	77.53

Clearly, the four steels studied in this work exhibit a moderate level of anisotropic effective elastic behavior, where both their Young's modulus and the Poisson's ratios depend on orientation with respect to the sheet loading direction. As has been determined, the individual crystals exhibit the crystalline anisotropy and symmetry. The contour plots presented in Fig. 3 reveal the level of orientation dependence of Young's modulus for ferrite and martensite in 3D. Interestingly, soft vs. stiff directions are the opposite for the two phases. Moreover, the levels of elastic anisotropy are different. The estimated Zener anisotropy ratio, $A = \frac{2C_{44}}{C_{11}-C_{12}}$, for ferrite is $A = 2.0$, which is slightly less than the value for Fe ($A = 2.4$ for Fe). While a value of 1.0 for A is for an isotropic material, that value for martensite is $A = 0.95$. The values of the constants and the small level of anisotropy we obtain for martensite are in good agreement with the experimental measurements presented in [52], which are given in table A4 of the Appendix A. The effective behavior of polycrystalline aggregates of these steels is a direct consequence of texture and phase fractions, homogenizing the crystalline effects.

In closing, we reflect on possible sources influencing the accuracy of the predictions, in addition to the intrinsic assumptions involved in the homogenization approached we employed to estimate the effective properties. We have used EBSD and SEM to initialize texture and phase fraction input to the models. While we have attempted to provide as statistically significant as possible data based on these techniques, it is possible that spatial variation in the microstructure of studied steels can cause these to be inaccurate. In particular, texture of martensite was assumed as uniform random. To relax this concern, future research will involve generating the input to the models based on the data collected using neutron diffraction. Neutron diffraction allows for the measurement of microstructural features averaged over large volumes due to the deep penetration of thermal neutrons into most materials combined with beam spot sizes of ~1 cm^2. The constants determined in this work asummed single chemical composition for ferrite and single chemical composition for martensite. The four studied steels have very similar chemical composition but not identical. Solute atoms could induce lattice strains, which could change lattice parameters. Such distortions could affect the single crystal elastic constants, and as a result, the effective behavior. For example, the studied steels have a slight difference in the content of carbon (C). C atoms within the interstitial sites increase the interatomic constants and should increase the stiffness on one hand. On the other hand, these atoms increase the volume of the lattice, reducing the stiffness. Thus, there are some competing effects [53] but considering the similarity in the composition of the studied steels, the effect on solute on the determined crystal constants is likely to be secondary. In addition, any variation in the density of dislocations, especially in martensite, can have some effect on the constants [54].

5. Conclusions

This work has shown that it is possible to reliably estimate single crystal stiffness coefficients for ferrite and martensite using an approach involving single crystal mechanics, homogenization theories, microstructural characterization data, and orientation dependent Young's modulus and Poisson's ratio data. The microstructure data of DP 590 and MS 1700 steels was used to initialize the homogenization models in terms of texture and phase fraction. The models were run within an optimization scheme to extract the single crystal stiffness constants for ferrite and martensite, while reproducing the effective property data. Subsequently, the constants were verified by predicting the effective property data for DP 980 and DP 1180. It is shown that the model taking the calibrated constants and microstructure as input can predict the effective elastic properties for all studied steels containing various levels of martensitic volume fraction. The effective behavior of the predominantly martensitic steel, MS 1700, was predicted as nearly isotropic due to nearly isotropic behavior of a martensite single crystal. In contrast, the behavior of the predominantly ferrite steel, DP 590, was predicted as the most anisotropic amongst the studied steels, as a consequence of anisotropic behavior of a ferrite single crystal and texture. Thus, the effective behavior of steels exhibiting a different level of anisotropy was successfully predicted. Since the effective elastic stiffness estimated using the full-field FFT solver of several microstructural realizations, for constant texture and phase fractions and the SC approach for the same texture and phase fraction, were nearly identical, it is inferred that texture and phase fractions play a primary role in governing the effective elastic behaviors of steels, while grain, phase, and misorientation distributions are secondary. The results of this work represent a significant incentive to introduce elastic anisotropy in numerical tools for simulating metal forming processes of dual-phase steels using the texture informed crystal mechanics-based models to more accurately estimate the effective elastic properties required by such simulations. Furthermore, texture evolution can be simulated during a forming process using crystal plasticity models such as EPSC and EVPFFT implying that the evolution of the effective elastic behavior with plastic strain is also calculated during the forming process.

Acknowledgments

This research was sponsored by the U.S. National Science Foundation and was accomplished under the CAREER grant no. CMMI-1650641. The authors also acknowledge discussions with Professor Yannis P. Korkolis of the University of New Hampshire and Dr. Ricardo A. Lebensohn of Los Alamos National Laboratory.

Appendix A

This appendix presents a summary of available single crystal elastic coefficients for α-Iron (Fe), ferrite, and martensite, including the source of the values. (Tables A1–A5)

Table A1
Single crystal elastic stiffness coefficients in GPa for α-iron (Fe) measured using either the ultrasonic pulse-echo technique or resonant ultrasonic spectroscopy at room temperature (~300 K) and atmospheric pressure.

Source	C_{11}	C_{12}	C_{44}
[55]	236.88	140.63	116.01
[56]	241.50	146.63	111.73
[57]	228.09	133.48	110.86
[58]	209.36	113.66	111.36
[59]	242.00	146.50	112.00
[59]	237.00	141.00	116.00
[60]	233.10	135.44	117.83
[61]	228.00	132.00	116.50
[61]	223.00	127.00	115.00
[62]	231.40	134.70	116.40
[63]	230.10	134.60	116.60
[64]	226.00	140.00	116.00
[65]	232.20	135.60	117.00
[52]	231.50	135.00	116.00
[66]	230.37	134.07	115.87

Table A2
Single crystal elastic stiffness coefficients in GPa for α-iron estimated theoretically using first-principles calculations based on density functional theory (DFT) methods.

Source	C_{11}	C_{12}	C_{44}
[67]	276.6	145.8	97.58
[68]	289	118	115
[69]	279	140	99
[70]	271	145	101
[71]	303	150	126
[72]	297.8	141.9	106.7
[73]	279.2	148.8	93.0

Table A3
Single crystal elastic stiffness coefficients in GPa for ferrite, estimated theoretically using a micromechanical approach involving a crystallography-based anisotropic thermomechanical continuum model.

Source	C_{11}	C_{12}	C_{44}
[74]	233.3	135.5	118.0

Table A4
Elastic stiffness tensor values in GPa for martensite measured using resonant ultrasonic spectroscopy at room temperature (∼300 K) and atmospheric pressure.

Source	C_{1111}	C_{2222}	C_{3333}	C_{1122}	C_{1133}	C_{2233}	C_{2323}	C_{3131}	C_{1212}
[52]	268.1	268.4	267.2	111.2	110.2	111.0	79.06	78.72	78.85

Table A5
Single crystal elastic stiffness coefficients in GPa for martensite, estimated theoretically using either a micromechanical approach involving a crystallography-based anisotropic thermomechanical continuum model or DFT.

Source	C_{11}	C_{12}	C_{44}
[74]	372.4	345.0	191.0
[75]	417.4	242.4	211.1
[67]	268.1	139.7	89.2
[67]	259.0	135.2	86.6
[76]	278.0	148.0	98.0

Appendix B

This appendix presents values of the elastic stiffness tensor components in MPa for the four steels based on the single crystal elastic coefficients established in this paper and their measured texture and phase fractions.

C	DP 590	DP 980	DP 1180	MS 1700
C_{1111}	260,080.22	262,883.38	264,902.01	277,435.51
C_{1122}	91,758.80	101,380.85	103,506.58	116,707.88
C_{1133}	98,082.99	102,394.45	104,378.27	116,758.64
C_{1112}	373.81	−81.34	−71.79	−15.04
C_{1113}	391.75	−11.71	−12.44	−16.48
C_{1123}	352.26	−225.35	−192.98	0.07
C_{2222}	262,349.70	266,081.14	267,659.45	277,644.75
C_{2233}	95,813.51	99,196.68	101,620.84	116,549.40
C_{2212}	409.71	−24.34	−21.53	−5.63
C_{2213}	20.52	−141.35	−123.20	−18.00
C_{2223}	111.68	418.16	362.49	33.63
C_{3333}	256,025.51	265,067.54	266,787.76	277,593.99
C_{3312}	−783.52	105.68	93.31	20.67
C_{3313}	−412.27	153.06	135.64	34.48
C_{3323}	−463.95	−192.82	−169.50	−33.70
C_{1212}	75,445.64	79,396.14	79,527.72	80,283.19
C_{1213}	350.19	−227.27	−194.40	0.08
C_{1223}	23.95	−135.84	−119.04	−17.95
C_{1313}	81,503.84	80,386.05	80,381.80	80,333.89
C_{1323}	−809.71	103.53	91.66	20.63
C_{2323}	79,275.37	77,303.06	77,710.09	80,125.18

References

[1] Nye JF. Physical properties of crystals: their representation by tensors and matrices. New York, USA: Oxford university press; 1985.
[2] Knezevic M, Crapps J, Beyerlein IJ, Coughlin DR, Clarke KD, McCabe RJ. Anisotropic modeling of structural components using embedded crystal plasticity constructive laws within finite elements. Int J Mech Sci 2016;105:227–38.
[3] Kocks UF, Tomé CN, Wenk H-R. Texture and anisotropy. Cambridge, UK: Cambridge University Press; 1998.
[4] Verma RK, Kuwabara T, Chung K, Haldar A. Experimental evaluation and constitutive modeling of non-proportional deformation for asymmetric steels. Int J Plast 2011;27:82–101.
[5] Hasegawa T, Yakou T, Karashima S. Deformation behaviour and dislocation structures upon stress reversal in polycrystalline aluminium. Mater Sci Eng 1975;20:267–76.
[6] Zecevic M, Knezevic M. A dislocation density based elasto-plastic self-consistent model for the prediction of cyclic deformation: application to Al6022-T4. Int J Plast 2015;72:200–17.
[7] Pavlina E, Lee M-G, Barlat F. Observations on the nonlinear unloading behavior of advanced high strength steels. Metall Mater Trans A 2015;46:18–22.
[8] Wagoner RH, Lim H, Lee M-G. Advanced issues in springback. Int J Plast 2013;45:3–20.
[9] Sumikawa S, Ishiwatari A, Hiramoto J, Urabe T. Improvement of springback prediction accuracy using material model considering elastoplastic anisotropy and Bauschinger effect. J Mater Process Technol 2016;230:1–7.
[10] Turner PA, Tomé CN. A study of residual stresses in Zircaloy-2 with rod texture. Acta Metall Mater 1994;42:4143–53.
[11] Ghorbanpour S, Zecevic M, Kumar A, Jahedi M, Bicknell J, Jorgensen L, Beyerlein IJ, Knezevic M. A crystal plasticity model incorporating the effects of precipitates in superalloys: application to tensile, compressive, and cyclic deformation of Inconel 718. Int J Plast 2017;99:162–85.
[12] Zecevic M, Knezevic M, Beyerlein IJ, Tomé CN. An elasto-plastic self-consistent model with hardening based on dislocation density, twinning and de-twinning: application to strain path changes in HCP metals. Mater Sci Eng A 2015;638:262–74.
[13] Lebensohn RA, Kanjarla AK, Eisenlohr P. An elasto-viscoplastic formulation based on fast Fourier transforms for the prediction of micromechanical fields in polycrystalline materials. Int J Plast 2012;32–33:59–69.
[14] Eghtesad A, Barrett TJ, Germaschewski K, Lebensohn RA, McCabe RJ, Knezevic M. OpenMP and MPI implementations of an elasto-viscoplastic fast Fourier transform-based micromechanical solver for fast crystal plasticity modeling. Adv Eng Software 2018;126:46–60.
[15] Hill R. The elastic behavior of a crystalline aggregate. Proceedings of the royal society of London. Series A, Mathematical and physical sciences 1952;65:349–54.
[16] Hill R. Elastic properties of reinforced solids: some theoretical principles. J Mech Phys Solids 1963;11:357–72.
[17] Paul B. Prediction of elastic constants of multiphase materials. Trans Metall Soc AIME 1960;218:36–41.
[18] Knezevic M, Kalidindi SR. Fast computation of first-order elastic-plastic closures for polycrystalline cubic-orthorhombic microstructures. Comput Mater Sci 2007;39:643–8.
[19] Landry N, Knezevic M. Delineation of first-order elastic property closures for hexagonal metals using fast fourier transforms. Materials 2015;8:6326–45.
[20] Wu X, Proust G, Knezevic M, Kalidindi SR. Elastic-plastic property closures for hexagonal close-packed polycrystalline metals using first-order bounding theories. Acta Mater. 2007;55:2729–37.
[21] Kalidindi SR, Knezevic M, Niezgoda S, Shaffer J. Representation of the orientation distribution function and computation of first-order elastic properties closures using discrete Fourier transforms. Acta Mater 2009;57:3916–23.
[22] Fast T, Knezevic M, Kalidindi SR. Application of microstructure sensitive design to structural components produced from hexagonal polycrystalline metals. Comput Mater Sci 2008;43:374–83.
[23] Voigt W. Lehrbuch der Krystallphysik. Teubner xxiv 1910.
[24] Lebensohn RA. N-site modeling of a 3D viscoplastic polycrystal using Fast Fourier Transform. Acta Materialia 2001;49:2723–37.
[25] Lebensohn RA, Kanjarla AK, Eisenlohr P. An elasto-viscoplastic formulation based on fast Fourier transforms for the prediction of micromechanical fields in polycrystalline materials. Int J Plast 2012;32-33:59–69.
[26] Lipinski P, Berveiller M. Elastoplasticity of micro-inhomogeneous metals at large strains. Int J Plast 1989;5:149–72.
[27] Eshelby JD. The determination of the elastic field of an ellipsoidal inclusion, and related problems. Proc R Soc Lond A 1957;241:376–96.
[28] Zecevic M, Knezevic M. Latent hardening within the elasto-plastic self-consistent polycrystal homogenization to enable the prediction of anisotropy of AA6022-T4 sheets. Int J Plast 2018;105:141–63.
[29] Lebensohn RA, Turner PA, Signorelli JW, Canova GR, Tomé CN. Calculation of intergranular stresses based on a large-strain viscoplastic self-consistent polycrystal model. Modell Simul Mater Sci Eng 1998;6:447.
[30] Diard O, Leclercq S, Rousselier G, Cailletaud G. Distribution of normal stress at grain boundaries in multicrystals: application to an intergranular damage modeling. Comput Mater Sci 2002;25:73–84.
[31] Jahedi M, Ardeljan M, Beyerlein IJ, Paydar MH, Knezevic M. Enhancement of orientation gradients during simple shear deformation by application of simple compression. J Appl Phys 2015;117:214309.
[32] Ardeljan M, McCabe RJ, Beyerlein IJ, Knezevic M. Explicit incorporation of deformation twins into crystal plasticity finite element models. Comput Methods Appl Mech Eng 2015;295:396–413.
[33] Zhao Z, Ramesh M, Raabe D, Cuitiño AM, Radovitzky R. Investigation of three--dimensional aspects of grain-scale plastic surface deformation of an aluminum oligocrystal. Int J Plast 2008;24:2278–97.
[34] Ardeljan M, Knezevic M. Explicit modeling of double twinning in AZ31 using crystal plasticity finite elements for predicting the mechanical fields for twin variant selection and fracture analyses. Acta Mater 2018;157:339–54.
[35] Ardeljan M, Beyerlein IJ, Knezevic M. Effect of dislocation density-twin interactions on twin growth in AZ31 as revealed by explicit crystal plasticity finite element modeling. Int J Plast 2017;99:81–101.
[36] Knezevic M, Levinson A, Harris R, Mishra RK, Doherty RD, Kalidindi SR. Deformation twinning in AZ31: Influence on strain hardening and texture evolution. Acta Mater 2010;58:6230–42.

[37] Zecevic M, Korkolis YP, Kuwabara T, Knezevic M. Dual-phase steel sheets under cyclic tension–compression to large strains: experiments and crystal plasticity modeling. J Mech Phys Solids 2016;96:65–87.

[38] Bunge H-J. Texture analysis in materials science. Mathematical methods. Göttingen: Cuvillier Verlag; 1993.

[39] Ray R, Jonas JJ, Hook R. Cold rolling and annealing textures in low carbon and extra low carbon steels. Int Mater Rev 1994;39:129–72.

[40] Randle V, Engler O. Introduction to texture analysis. Macrotexture, microstructure & orientation mapping. Gordon and Breach Science Publishers; 2000.

[41] Von Schlippenbach U, Emren F, Lücke K. Investigation of the development of the cold rolling texture in deep drawing steels by ODF-analysis. Acta Metallurgica 1986;34:1289–301.

[42] Lücke K, Hölscher M. Rolling and recrystallization textures of BCC steels. Texture, Stress, Microstruct 1991;14:585–96.

[43] Knezevic M, Nizolek T, Ardeljan M, Beyerlein IJ, Mara NA, Pollock TM. Texture evolution in two-phase Zr/Nb lamellar composites during accumulative roll bonding. Int J Plast 2014;57:16–28.

[44] Jahedi M, Paydar MH, Zheng S, Beyerlein IJ, Knezevic M. Texture evolution and enhanced grain refinement under high-pressure-double-torsion. Mater Sci Eng A 2014;611:29–36.

[45] Smith DH, Bicknell J, Jorgensen L, Patterson BM, Cordes NL, Tsukrov I, Knezevic M. Microstructure and mechanical behavior of direct metal laser sintered Inconel alloy 718. Mater Charact 2016;113:1–9.

[46] Eghtesad A, Barrett TJ, Knezevic M. Compact reconstruction of orientation distributions using generalized spherical harmonics to advance large-scale crystal plasticity modeling: Verification using cubic, hexagonal, and orthorhombic polycrystals. Acta Mater 2018;155:418–32.

[47] Knezevic M, Landry NW. Procedures for reducing large datasets of crystal orientations using generalized spherical harmonics. Mech Mater 2015;88:73–86.

[48] Pinard PT, Schwedt A, Ramazani A, Prahl U, Richter S. Characterization of dual-phase steel microstructure by combined submicrometer EBSD and EPMA carbon measurements. Microsc Microanal 2013;19:996–1006.

[49] Deng N, Korkolis YP. Elastic anisotropy of dual-phase steels with varying martensite content. Int J Solids Struct 2018;141-142:264–78.

[50] Deng N, Korkolis YP. Determination of the shear modulus of orthotropic thin sheets with the anticlastic-plate-bending experiment. J Eng Mater Technol 2018;140:041011–041011-041017.

[51] Groeber MA, Jackson MA. DREAM. 3D: a digital representation environment for the analysis of microstructure in 3D. Integr Mater Manufact Innovat 2014;3:5.

[52] Kim SA, Johnson WL. Elastic constants and internal friction of martensitic steel, ferritic-pearlitic steel, and α-iron. Mater Sci Eng A 2007;452:633–9.

[53] Ledbetter H, Austin M. Effects of carbon and nitrogen on the elastic constants of AISI type 304 stainless steel. Mater Sci Eng 1985;70:143–9.

[54] Granato AV, Lücke K. Theory of mechanical damping due to dislocations. J Appl Phys 1956;27:583–93.

[55] Goens E, Schmid E. Über die elastische Anisotropie des Eisens. Naturwissenschaften 1931;19:520–4.

[56] Kimura R, Ohno K. On the elastic constants of single crystals of iron. Sci Rept Tohoku Univ 1934;23:359–64.

[57] Kimura RI. On the elastic moduli of ferromagnetic materials. Part I. Dynamical measurements of the elastic morduli of iron crystals. Nippon Sugaku-Buturigakkwai Kizi Dai 3 Ki 1939;21:686–706.

[58] Kimura RI. On the elastic moduli of ferromagnetic materials. Part II. The change in Young's modulus, due to magnetisation and temperature. Proc Physico-Math Soc Jpn 3rd Ser 1939;21:786–99.

[59] Alexandrov KS, Ryzhova TV. The elastic properties of crystals. Soviet Phys-Crystallograp 1961;6:228–52.

[60] Rayne JA, Chandrasekhar BS. Elastic constants of Iron from 4.2 to 300°K. Phys Rev 1961;122:1714–16.

[61] Lord AEJ, Beshers DN. Elastic stiffness coefficients of Iron from 77° to 673°K. J Appl Phys 1965;36:1620–3.

[62] Rotter CA, Smith CS. Ultrasonic equation of state of iron: I. low pressure, room temperature. J Phys Chem Solids 1966;27:267–76.

[63] Guinan MW, Beshers DN. Pressure derivatives of the elastic constants of α-iron to 10 kbs. J Phys Chem Solids 1968;29:541–9.

[64] Leese J, Lord A Jr. Elastic stiffness coefficients of single-crystal iron from room temperature to 500 °C. J Appl Phys 1968;39:3986–8.

[65] Dever D. Temperature dependence of the elastic constants in α-iron single crystals: relationship to spin order and diffusion anomalies. J Appl Phys 1972;43:3293–301.

[66] Adams JJ, Agosta D, Leisure R, Ledbetter H. Elastic constants of monocrystal iron from 3–500 K. J Appl Phys 2006;100:113530.

[67] Souissi M, Numakura H. Elastic Properties of Fe–C and Fe–N Martensites. ISIJ Int 2015;55:1512–21.

[68] Vočadlo L, de Wijs GA, Kresse G, Gillan M, Price GD. First principles calculations on crystalline and liquid iron at Earth's core conditions. Faraday Discuss 1997;106:205–18.

[69] Guo G, Wang H. Gradient-corrected density functional calculation of elastic constants of Fe, Co and Ni in bcc, fcc and hcp structures. Chin J Phys 2000;38:949–61.

[70] Caspersen KJ, Lew A, Ortiz M, Carter EA. Importance of Shear in the bcc-to-hcp transformation in Iron. Phys Rev Lett 2004;93:115501.

[71] Sha X, Cohen RE. First-principles thermoelasticity of bcc iron under pressure. Phys Rev B 2006;74:214111.

[72] Zhang H, Johansson B, Vitos L. Ab initio calculations of elastic properties of bcc Fe-Mg and Fe-Cr random alloys. Phys Rev B 2009;79:224201.

[73] Shang SL, Saengdeejing A, Mei ZG, Kim DE, Zhang H, Ganeshan S, Wang Y, Liu ZK. First-principles calculations of pure elements: equations of state and elastic stiffness constants. Comput Mater Sci 2010;48:813–26.

[74] Tjahjanto DD, Turteltaub S, Suiker ASJ. Crystallographically based model for transformation-induced plasticity in multiphase carbon steels. Continuum Mech Thermodyn 2008;19:399–422.

[75] Tasan CC, Diehl M, Yan D, Zambaldi C, Shanthraj P, Roters F, Raabe D. Integrated experimental–simulation analysis of stress and strain partitioning in multiphase alloys. Acta Mater 2014;81:386–400.

[76] Fellinger MR, Hector LG, Trinkle DR. Effect of solutes on the lattice parameters and elastic stiffness coefficients of body-centered tetragonal Fe. Comput Mater Sci 2018;152:308–23.